



Research Signpost  
37/661 (2), Fort P.O.  
Trivandrum-695 023  
Kerala, India

Recent Developments in Wear Prevention, Friction and Lubrication, 2010: 279-314  
ISBN: 978-81-308-0377-7 Editor: George K. Nikas

## 8. Surface characterization, adhesion measurements and modeling of microelectromechanical systems

Xiaojie Xue\* and Andreas A. Polycarpou

*Department of Mechanical Science and Engineering, University of Illinois at Urbana-Champaign, 1206 West Green Street, Urbana, Illinois 61801, USA*

**Abstract.** Adhesion, also referred to as stiction, is a common failure mechanism occurring in microelectromechanical systems (MEMS) during device fabrication and operation and has become the main barrier to the advancement and wide commercialization of MEMS and miniature devices. To investigate the adhesion behavior of MEMS devices, experimentally and theoretically, different small scale interfacial experiments and continuum-based models have been developed and applied with varying success to explain such phenomena. In this work, a beam-peel-based MEMS experimental setup was designed and built to measure the adhesion energy between MEMS microcantilevers and a substrate at different humidity levels. The microcantilever arrays were separated from the substrate and their fixed ends were directly attached to a piezoactuator to control the beam displacement with sub-nanometer accuracy. The experimental setup was sealed in a chamber with precise humidity control. An in-situ interferometer was used to measure the beam deflection and crack length during the peel test. To examine the effects of surface roughness and relative humidity on adhesion energy, different surface pairs were measured at humidity levels ranging from 40% to 92%. Before testing, the microcantilevers and substrates were scanned using an Atomic Force Microscope (AFM). Surface roughness parameters and the exact probability density function of the asperity heights were extracted and directly entered into a statistical-based roughness model. An Extended-Maugis-Dugdale (EMD) single-asperity meniscus model considering both asperity deformation and solid surface interaction was coupled with the Pearson surface statistical model to develop an improved elastic asymmetrical surface meniscus model. The model compared favorably with the experimental data.

\* Currently with Analog Devices Inc.

Correspondence/Reprint request: Professor Andreas A. Polycarpou, Department of Mechanical Science and Engineering, University of Illinois at Urbana-Champaign, 1206 West Green Street, Urbana, Illinois 61801, USA  
E-mail: polycarp@illinois.edu

## Introduction

By integrating mechanical elements, sensors, actuators, and electronics on a common silicon substrate, Micro-Electro-Mechanical Systems (MEMS) reduce cost, size, weight, and power consumption while increasing performance, production volume, and functionality by orders of magnitude [1]. However, due to the relatively high compliance of micromachined components, large surface-to-volume ratios, and small surface separation distances, surface forces such as van der Waals, capillary, and hydrogen bonding, become dominant over body forces or restoring forces (stiffness of the freestanding microstructures) causing suspended MEMS structures to deflect towards the substrate and even permanently adhere. This phenomenon is called *adhesion*, which is sometimes referred to as *stiction* in the MEMS literature.

Adhesion can occur during the final stage of the micromachining process (release adhesion), during normal operation (in-use adhesion) [2], or while parts are stored (dormancy adhesion). Release adhesion is very common in sacrificial surface micromachining as this type of manufacturing requires the chemical wet-etch of the sacrificial layer and several liquid rinse steps before the device becomes operable. When the device is taken out of the final rinse solution, the remaining liquid trapped between the compliant MEMS structures and the surface below results in strong capillary force pulling the suspended structures down to the substrate. In-use adhesion occurs during normal operation of MEMS devices and can be caused by liquids, especially water from the environment that condenses on the device surfaces [3], mechanical shock, or “over range” input signals. Moreover, some MEMS applications, e.g. a microengine [4], a digital-micro-display (DMD) [5], accelerometer [6] and RF MEMS switch [7], involve surface contact and sliding, which may cause adhesion failures and hinder normal operation of the devices. Dormancy adhesion relates to an adhesion failure that occurs while the device is stored and may be caused by environmental conditions such as humidity [8].

Clearly adhesion is a common failure mechanism occurring in MEMS devices, a major reliability concern, and a barrier to widely commercializing MEMS devices. In order to increase the MEMS fabrication yield and long-term durability, significant efforts have been made to investigate adhesion behavior experimentally and theoretically, e.g., [9-11], to alleviate adhesion problems in MEMS devices, e.g. [12-15], and to repair adhesion-failed devices, e.g. [16, 17].

Adhesion and interaction between a single asperity and a flat surface have mainly been examined by surface force apparatus (SFA) [18] and atomic force microscopy (AFM) [19]. Since adhesion behavior is directly related to the surface energy, a more convenient parameter, *adhesion energy*, is usually used to evaluate

the interaction between two approaching surfaces. A number of techniques have been explored to experimentally study the adhesion behavior between two rough surfaces. The cantilever beam array technique presented by Mastrangelo and Hsu [20] is the most widely used method, in which the adhesion energy is determined by the length of the shortest adhered beam. de Boer and Michalske [21] expanded on this approach and developed a fracture mechanics model to determine the adhesion energy. Using the cantilever array technique, DelRio *et al.* [22] experimentally investigated the adhesion as a function of relative humidity and surface roughness. Jones *et al.* [23] presented experiments and models to examine the adhesion of microcantilevers by means of mechanical actuation. Leseman *et al.* [24] developed an experimental technique termed “beam-peel-test” to measure the effects (under laboratory ambient conditions) of deionized (DI) water and isopropyl alcohol (IPA) on release adhesion, where the microcantilevers were peeled from the substrate using a piezoelectric actuator and the crack length was measured to calculate the adhesion energy.

In addition to cantilever beam array methods, other techniques have also been explored to investigate the in-plane adhesion in MEMS, for example the doubly clamped cantilever beam array presented by Legtenberg *et al.* [25] and the symmetric folded-beam butterfly suspension developed by Alley *et al.* [26]. Moreover, besides the contact between the bottom surface of MEMS structures and the ground surface (in-plane contact), many MEMS applications such as the microengine involve contact between vertical surfaces (sidewalls). A sidewall adhesion tester was developed by Ashurst *et al.* [27] to measure the sidewall adhesion.

Adhesion forces between two rough surfaces in close proximity or contacting each other may arise due to van der Waals, capillary, and electrostatic forces. In a dry environment, the van der Waals interaction usually determines the adhesion behavior of microstructures. Based on the Greenwood and Williamson (GW) statistical roughness model [28], several continuum mechanics-based adhesive models have been proposed based on asperity interactions at various separation regimes. Chang *et al.* [29] developed an adhesion model (CEB model) for rough surfaces under dry contact conditions by combining the IDMT (improved Derjaguin-Muller-Toporov) model [30] with an extended GW model that included elastic-plastic contacts. Kogut and Etsion [31] developed a rough surface adhesion model (KE model) based on their improved single-asperity (finite element-based) model [32]. An advantage of both CEB and KE models is that they are valid for elastic-plastic contact conditions. However, a major drawback of these models is that since they are based on the IDMT adhesion model, they are only valid for a limited range of low adhesion parameter values. Combining the Extended-Maugis-Dugdale (EMD) model [33] and the ISBL (improved sub-boundary lubrication)

model [34], Shi and Polycarpou [35] proposed an elastic-plastic hybrid “dry” adhesion model for rough contacting surfaces which is valid for elastic-plastic contacts and for the entire range of adhesion parameter values.

At high relative humidity ( $RH$ ) values, the meniscus force due to capillary condensation becomes dominant. Incorporating different single-asperity models into the Greenwood-Williamson statistical model [28], several meniscus models have been presented to predict the effects of surface roughness/texture, lubricant film thickness, and environmental humidity. Based on Israelachvili’s single-asperity capillary model [36], Li and Talke [37] explored the effect of humidity on the adhesion force for multi-asperity contacts using the GW statistical model. Assuming liquid volume conservation, Tian and Matsudaira [38] presented an improved meniscus model for head-disk interfaces (HDIs) covered with a uniform liquid layer. Gao *et al.* [39] proposed yet another model to calculate the adhesion force between a sphere and a lubricated flat surface based on energy change considerations. Taking into account the local redistribution of molecularly thin lubricant, Gui and Marchon [40] proposed a meniscus-based static friction (stiction) model for HDIs. Interestingly, despite the numerous improvements in the abovementioned models, they do not specifically consider the change of the projected meniscus area due to the solid asperity deformation when contacting with the flat solid surface. The meniscus force between the contacting asperities was treated as a constant value independent of the spherical interference. Therefore, these multi-asperity meniscus models are valid only for high relative humidity levels ( $> 70\%$ ) and significantly underestimate the adhesion energy (or force) at intermediate and low humidity levels.

To fully analyze the adhesive contact interaction between two rough surfaces, a thorough understanding and modeling of single asperity/sphere adhesion contact is necessary. Fogden and White [41] extended the Hertz theory to analyze the elasticity of contacting spheres in the presence of capillary condensation. Zhang and Nakajima [42] analyzed the nanometer deformation of the sphere caused only by the Laplace pressure when “just contacting” with the flat surface. Xue and Polycarpou [43] developed a meniscus model for a deformable sphere on a rigid flat surface covering a large range of interference values from non-contact to a fully plastic contact. Using the extended-Maugis-Dugdale (EMD) theory, Xue and Polycarpou [44] presented a single-asperity capillary meniscus model considering asperity deformation due to both contact and adhesive forces.

A different modeling approach to predict adhesive forces in microsystems in the presence of molecularly thin lubricants has also been proposed using contact-mechanics based adhesion models. Incorporating the KE dry contact model [31] with the original sub-boundary lubrication (SBL) adhesion model [45], an alternative model termed improved SBL (ISBL) model [46] was presented to take

into account the presence of molecularly thin lubricant. However, in this model, the very thin lubricant strongly and uniformly adheres to the surface and the meniscus formation is energetically unfavorable. Thus, this model is not applicable for MEMS devices at high humidity levels and cannot capture the adhesion behavior in the presence of mobile lubricant in magnetic storage HDIs.

Since humidity is an important factor that greatly affects the meniscus force and adhesion behavior, the beam-peel-based experimental setup was improved to measure the adhesion energy between MEMS microcantilevers and different substrates at different humidity levels. The method allows measuring and comparing various substrates of different materials and surface topographies at controlled humidity levels using the same microcantilever arrays. Before testing, both the underside of the microcantilevers and the substrates were scanned using an AFM. The surface topographies were analyzed and surface roughness parameters including root-mean-square roughness ( $R_q$ ), skewness ( $S_{sk}$ ), kurtosis ( $S_{ku}$ ), areal density of asperities ( $\eta$ ), and average asperity radius ( $R$ ) were extracted. Also, the exact probability density function of the asperity heights was generated using the measured roughness parameters. The Extended-Maugis-Dugdale (EMD)-based single-asperity meniscus model [44] considering both the asperity deformation and solid surface interaction was coupled with the Pearson surface statistical model to develop an improved elastic asymmetrical surface meniscus model, which compared favorably with the experimental data.

## 1. MEMS surface characterization

All real surfaces are rough at the microscopic and submicroscopic scales. Contact between two rough surfaces occurs at discrete asperity summits. Surface forces are strong functions of surface properties and separation distance. To accurately analyze these interfacial forces and understand a system's overall behavior, it is necessary to investigate the micro-topography and mechanical properties of the opposing surfaces, especially surface roughness, and how it influences adhesion. A polycrystalline silicon (polysilicon) film of a few micrometers in thickness is the primary structural material for MEMS applications. For improved reliability of MEMS devices, different efforts have been made to characterize the polysilicon mechanical properties including surface roughness effects using different fabrication processes and surface treatments [47-50].

### 1.1. Sample fabrication

The microcantilevers used in this study were fabricated by Sandia National Laboratories using the 4-layer SUMMiT IV<sup>TM</sup> process [51]. It begins with single

side polished (SSP) n-type silicon wafers on which a 630 nm oxide layer is thermally grown. An 800 nm thick, low-stress, silicon nitride film is then deposited using low-pressure chemical vapor deposition (LPCVD), which is followed by depositing a 300 nm thick n-doped LPCVD polysilicon layer (referred to as *P0*) on the nitride layer. Then, a 2.0  $\mu\text{m}$  thick sacrificial oxide layer is deposited in an LPCVD furnace on the *P0* and patterned to provide an anchor for the microcantilevers. Two structural polysilicon layers, *P1* and *P2*, are deposited and patterned to create microcantilevers that are approximately 2.6  $\mu\text{m}$  thick. During the process known as “release etching,” the silicon dioxide layers between the polysilicon layers were completely etched away by soaking the sample in 49% hydrofluoric acid (HF) for 15 minutes, and then supercritical  $\text{CO}_2$  drying was used to obtain free-standing microcantilever arrays. To obtain a hydrophilic surface, the microcantilevers were then treated by oxygen plasma and the water contact angle on the treated surface was measured and found to be almost 0 degrees. After that, the die was scored and fractured along a line just beyond the anchor of the microcantilevers, generating a test sample with microcantilevers protruding freely beyond the anchor point, as shown in the optical and SEM images of Fig. 1. The number at the top of the beam arrays shows the beam length, 1500  $\mu\text{m}$ , the one at the bottom indicates the beam width, 30  $\mu\text{m}$ , and the numbers at the left represent the spacing between beams in the array, 2-100  $\mu\text{m}$ . The release steps described above are also listed in Table 1.

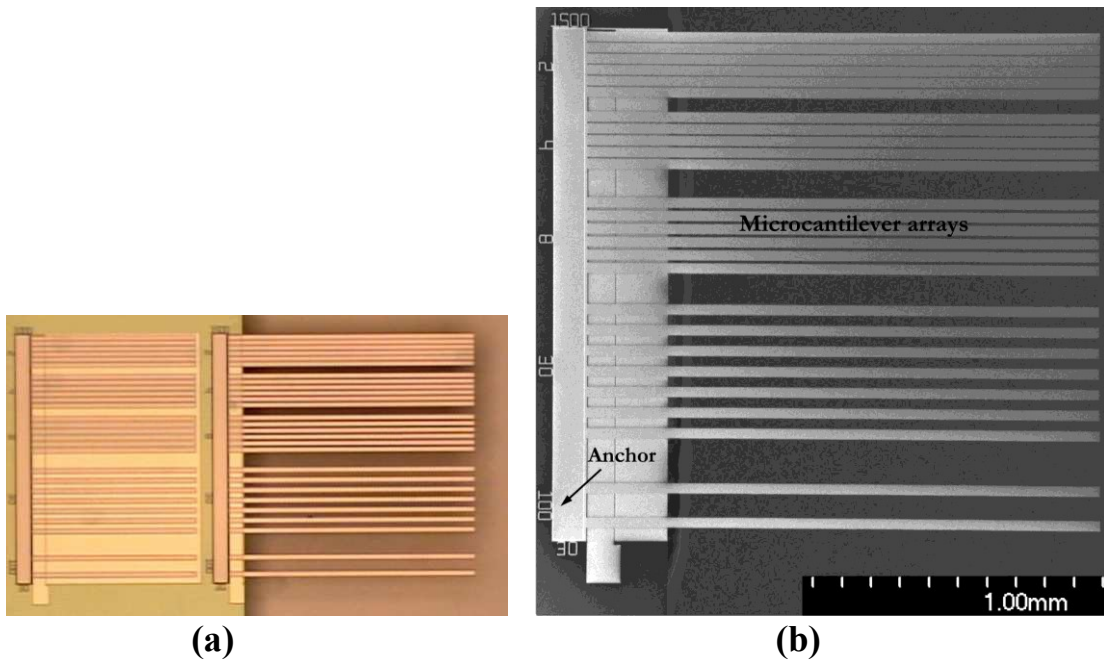


**Figure 1.** Array of 1500  $\mu\text{m}$  polysilicon microcantilevers. (a) optical image; (b) SEM image.

**Table 1** Microcantilever release procedure and sample preparation.

Step	Experimental Procedure
1	Acetone rinse for 30 min
2	IPA rinse for 10 min
3	DI water rinse for 10 min
4	49% hydrofluoric acid for 15 min
5	4:1 CH <sub>3</sub> OH:H <sub>2</sub> O rinse for 10 min
6	Pure CH <sub>3</sub> OH rinse for 10 min
7	Soak in pure CH <sub>3</sub> OH
8	Supercritical CO <sub>2</sub> dry
9	Oxygen plasma treatment
10	Separate microcantilevers from substrate

## 1.2. AFM measurements

In the LPCVD deposition process, parameters such as temperature, pressure, source gas dilution, and deposition time all greatly affect the structure and crystal growth of polysilicon which determine the mechanical and electrical properties of the film [52]. Since the surface roughness is an important geometrical surface property that directly affects adhesion and contact between two surfaces, in this study microcantilevers fabricated by two different runs were used to perform the experiments. The thicknesses of the microcantilevers from the first and second runs were measured to be 2.60  $\mu\text{m}$  and 2.55  $\mu\text{m}$ , respectively. Also, three types of substrates were used in this study, the first being non-doped single crystal silicon wafer, the second being polysilicon film deposited by LPCVD at a temperature of 585  $^{\circ}\text{C}$  for one hour and then annealed for 10 minutes, and the third being a rougher polysilicon substrate fabricated by LPCVD at 590  $^{\circ}\text{C}$  and annealed for 10 minutes. Both the microcantilevers and the substrates were treated by oxygen plasma before the peel experiments.

Due to the dependence on processing conditions and grain growth of polysilicon films, the surface topographical evolution and the roughness of the top and bottom surfaces in micro-fabricated MEMS are known to vary significantly [53]. To more accurately predict the adhesion behavior, the bottom surfaces of the microcantilevers and the substrates were measured using a tapping mode AFM with a root-mean-square noise resolution of 0.05 nm. For each surface, a sample area of 5x5  $\mu\text{m}^2$  was scanned at four different locations, which ensured at least 200 grains in each image. The data were repeatable and were digitized and exported for further processing. Using a graphics user interface program that extracts numerous

topographical parameters including the Birmingham-14 parameters [54], the following parameters were extracted: standard deviation of surface heights ( $R_q$ ), skewness ( $S_{sk}$ ), kurtosis ( $S_{ku}$ ), areal density of the asperities ( $\eta$ ), and average asperity radius ( $R$ ). The reduced skewness,  $S_{sk}$ , is a measure of the symmetry of the surface height distribution and the kurtosis,  $S_{ku}$ , is a measure of the concentration of the surface height distribution curve. For a Gaussian distribution,  $S_{sk} = 0$  and  $S_{ku} = 3$ . Note that the skewness and kurtosis of the asperity heights are the same as those of the surface heights, which has been experimentally verified [55]. The standard deviation of the asperity heights  $\sigma$  is related to the standard deviation of surface heights by [56]

$$R_q^2 = \sigma^2 + \frac{3.717 \times 10^{-4}}{\eta^2 R^2} \quad (1)$$

The validity Eq. (1), which was derived for a Gaussian distribution of asperity heights, has also been confirmed numerically for different roughness measurements [57].

Figure 2 depicts representative AFM images for different microcantilever bottom surfaces and substrates. It can be seen that the bottom surface of Run *B* is rougher than that of Run *A*, which could be caused by the LPCVD or the annealing processes. Based on the AFM measurements, the roughness parameters of the individual surfaces were extracted and are listed in the top part of Table 2. The  $R_q$  value of Run *B* is more than 2 times higher than that of Run *A*. Clearly, both types of beam surfaces display non-Gaussian distribution of the surface heights. An inaccurate prediction will be made if a Gaussian distribution is assumed for modeling and simulation, as discussed in section 3.3. For the substrates, it is clearly seen that the silicon wafer is much smoother than the LPCVD deposited polysilicon film, with 0.17 nm  $R_q$  for the silicon wafer, 5.5 nm  $R_q$  for polysilicon deposited at 585 °C, and 7.1 nm for polysilicon deposited at 590 °C. Again, similar to the case of the microcantilevers, the polysilicon substrate shows a non-Gaussian distribution. Note that a 392 nm high-pass filter was performed to remove the low-frequency components (waviness) and a 98 nm low-pass filter was used to eliminate the atomic noise, as discussed in [54]. Also, as discussed in [54], other ranges around these values could be used and the results would be similar.

Based on the AFM measurements, we see that for all five substrates, the areal asperity density is between 20.9 to 111.5 asperities per  $\mu\text{m}^2$ . In the experiment, the beam width is 30  $\mu\text{m}$  and only the data point with contact length no less than 200  $\mu\text{m}$  was used for the calculation. Therefore, the total number of asperities in the

contact area is at least  $1.2 \times 10^5$ , which assures the feasibility of using a statistical model to calculate the adhesion force and adhesion energy.

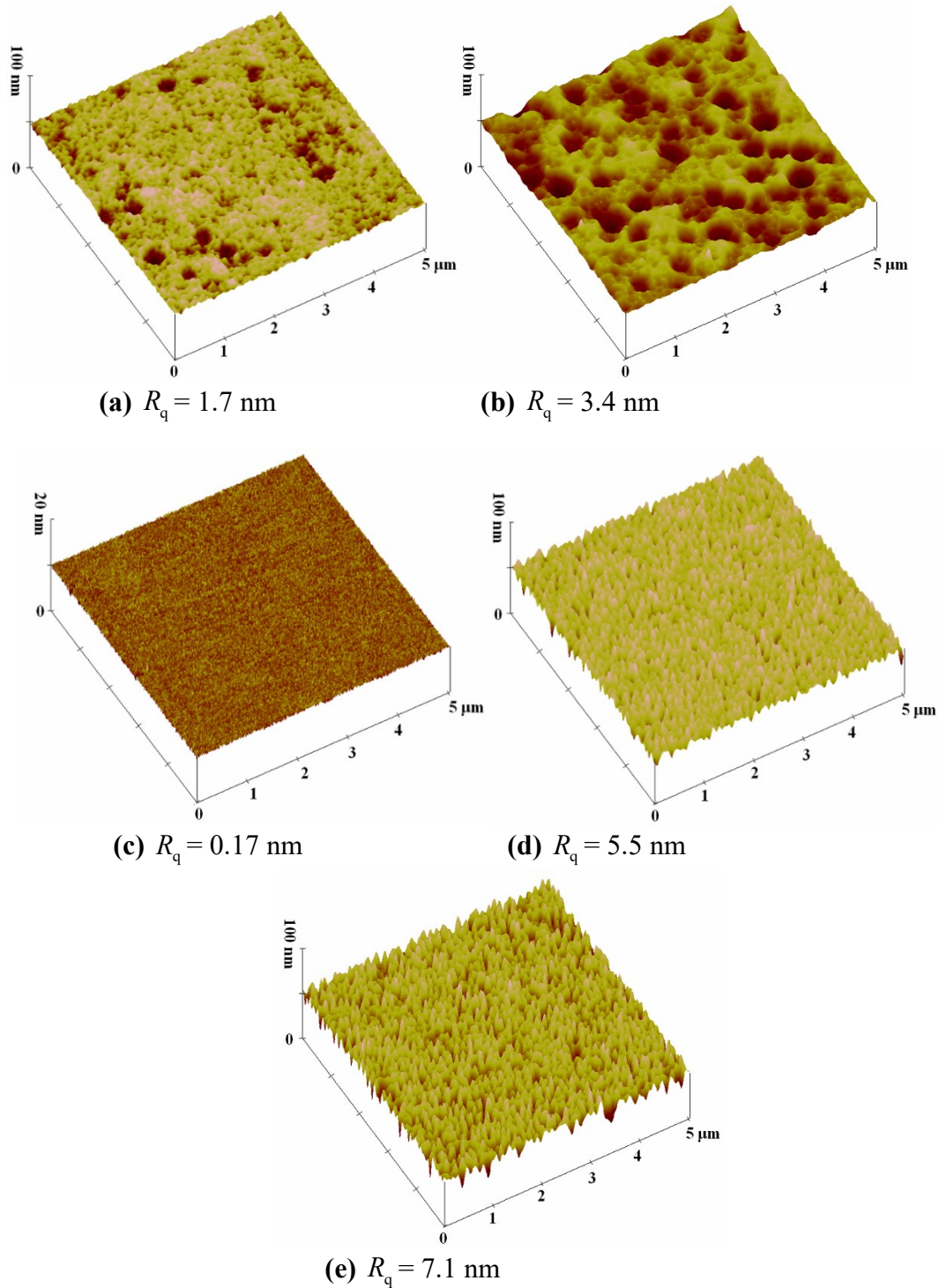


**Figure 2.** AFM images of bottom surfaces of microcantilevers fabricated by (a) Run *A* (b) Run *B*, (c) silicon wafer, (d) polysilicon film deposited by LPCVD at 585 °C, and (e) polysilicon film deposited by LPCVD at 590 °C.

**Table 2.** Measured individual and extracted combined surfaces roughness parameters.

Individual surface	Bottom surface of microcantilever		Substrate		
	1. Run <i>A</i>	2. Run <i>B</i>	3. Si	4. Polysilicon (LPCVD 585)	5. Polysilicon (LPCVD 590)
$R_q$ (nm)	1.7	3.4	0.17	5.5	7.1
$R$ ( $\mu\text{m}$ )	0.41	0.84	3.0	0.12	0.09
$\eta$ ( $1/\mu\text{m}^2$ )	67.9	20.9	111.5	48.0	49.4
$\sigma$ (nm)	1.5	3.3	0.16	4.2	5.5
$S_{sk}$	-0.78	-0.76	-0.31	-1.1	-0.73
$S_{ku}$	4.6	3.9	3.1	5.1	3.3
$\kappa$	0.38	-59.9	-0.74	1.6	-0.44
Surface type	IV	I	I	VI	I
Equivalent Rough Surface	Surface Pair				
	<i>a.</i> 1 vs 3	<i>b.</i> 2 vs 3	<i>c.</i> 1 vs 4	<i>d.</i> 1 vs 5	
$R_q$ (nm)	1.7	3.4	5.7	7.3	
$R$ ( $\mu\text{m}$ )	0.41	0.81	0.11	0.08	
$\eta$ ( $1/\mu\text{m}^2$ )	68.4	22.3	49.0	50.0	
$\sigma_{ab}$ (nm)	1.5	3.2	4.5	5.7	
$S_{sk}$	-0.77	-0.77	-0.86	-0.66	
$S_{ku}$	4.6	3.8	4.8	3.2	
$\kappa$	0.38	-5.2	0.49	-0.41	
Surface type	IV	I	IV	I	

$R_q$  = standard deviation of surface heights;

$R$  = average asperity radius;

$\eta$  = areal density of asperities;

$\sigma$  = standard deviation of asperity heights;

$\sigma_{ab}$  = standard deviation of asperity heights of the equivalent rough surface *ab*;

$S_{sk}$  = skewness;

$S_{ku}$  = kurtosis;  $\kappa$  = parameter in the Pearson system of frequency curves.

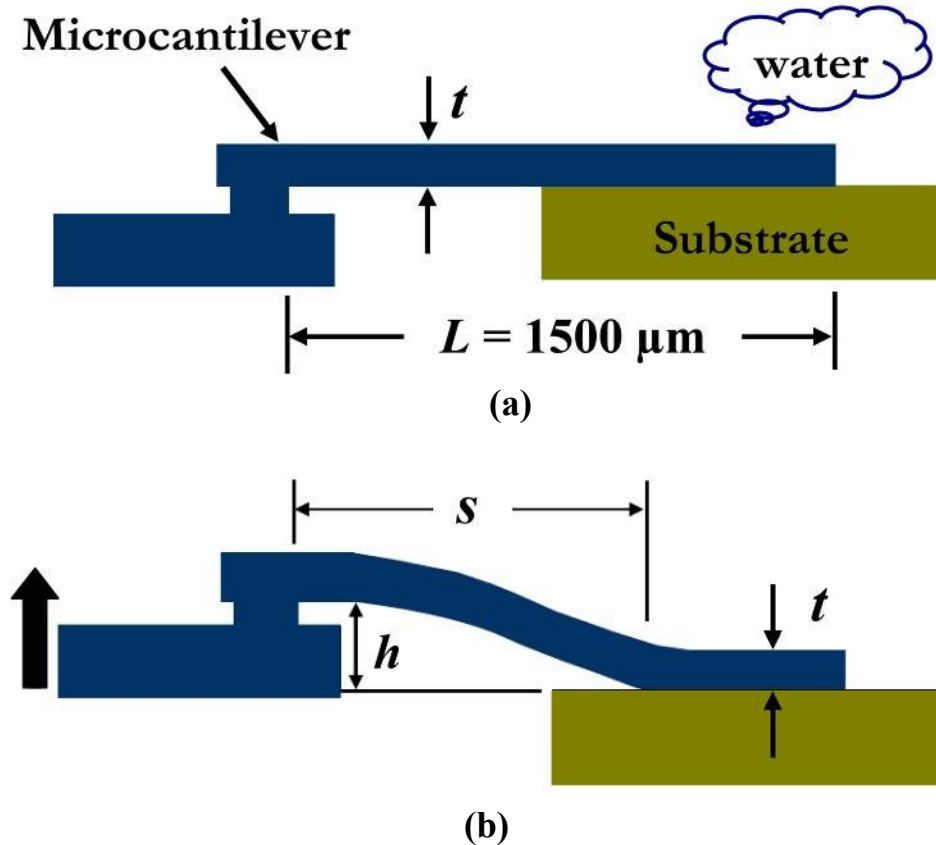


**Figure 3.** Schematic representation of experimental principle of the microcantilever peel test. (a) Microcantilever is aligned parallel to and tangent with the substrate, (b) as the anchor of the microcantilever is raised, the free-end of the beam sticks to the substrate, showing s-shape deformation.

## 2. Adhesion energy measurements

### 2.1. Experimental method

Figure 3 shows a schematic of the experimental principle: a series of microcantilevers are aligned to be parallel to the substrate and then lowered until just making contact with the substrate, as shown in Fig. 3(a). In the presence of capillary condensation, strong capillary forces arise between the bottom beam surface and the substrate. Note that the beams are very compliant as their dimensions are  $1500 \mu\text{m}$  long,  $2.6 \mu\text{m}$  thick, and  $30 \mu\text{m}$  wide. When the fixed end (the anchor) of the beams is raised gradually above the substrate, the free-end of the beams will be sticking to the substrate as shown with the s-shape deflection in Fig. 3(b), in which  $t$  is the thickness of the beam,  $L$  is the length of the beam,  $h$  is the height of the beam above the substrate, and  $s$  is the crack length, i.e. the portion

of the beam that is above the substrate (not stuck). de Boer and Michalske [21] modeled the adhered microcantilever substrate system using fracture mechanics. In this model, the crack driving force is given by the strain energy release rate,  $G$

$$G = -\frac{1}{w} \frac{dU}{ds} \quad (2)$$

where  $w$  is the width of the cantilever, and  $U$  is the strain energy. The crack resistance is the adhesion energy between the microcantilever and the substrate. The adhesion energy,  $\Gamma$ , is determined when the strain energy release rate equals the crack's resistance to propagation

$$G = \Gamma \quad (3)$$

For s-shaped beams, the elastic strain energy is given by [58]

$$U = \frac{6h^2 EI}{s^3} \quad (4)$$

where  $E$  is the Young's modulus of the cantilever beam, and  $I$  the moment of inertia of the cantilever. If the crack propagates without external work, the strain energy release rate  $G$  is given by

$$G = \frac{3}{2} \frac{h^2 Et^3}{s^4} \quad (5)$$

The above equations were derived assuming small strains arising from small beam deflections. Previous work [59] has shown that large deflection theory applies only when the end-deflection exceeds 30% of the beam length. As the end-deflections in the experiments performed in this work were always less than or equal to 10% of the beam length, the use of linear beam theory is justified.

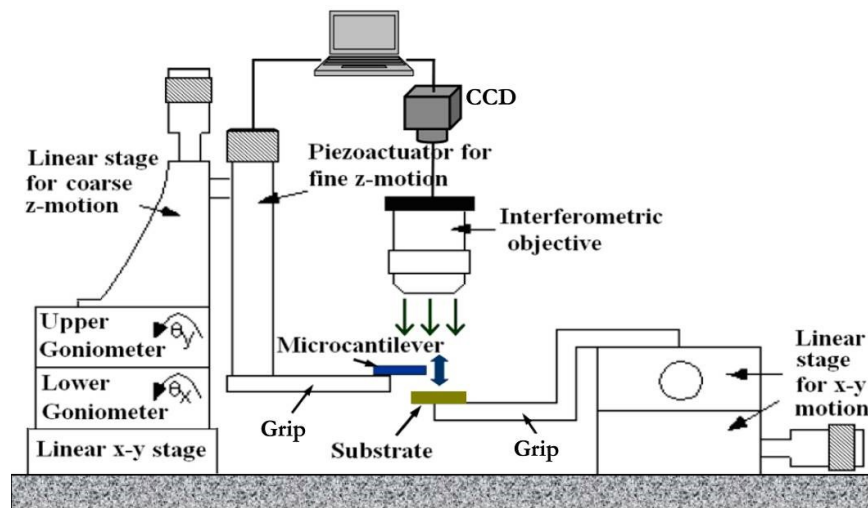
## 2.2. Experimental setup and procedure

Figure 4 depicts the schematic and actual photographs of the experimental apparatus. The microcantilever beam arrays are attached to a grip that is fixed to a piezoactuator (Physik Instrumente P845.60). The piezoactuator is connected to linear stages that allow for coarse movement in the X-Y directions as well as the

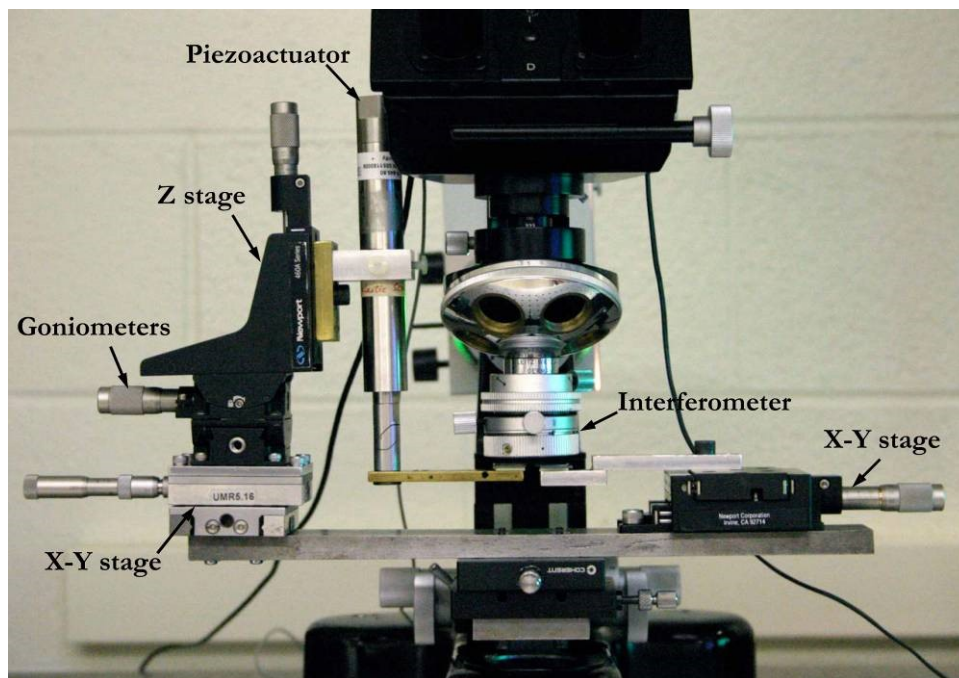
vertical Z direction. A computer connected to the piezoactuator accurately controls the vertical displacement of the microcantilevers with respect to the substrate. The piezoactuator has a vertical displacement range of 90  $\mu\text{m}$  with a resolution of 50 nm. The substrate is supported by another custom grip that is attached to a pair of stacked linear stages, and the X-Y stages are used to position the substrate below the microcantilever arrays. Two goniometers, mounted on the left between the linear Z-stage and the stacked X-Y stage, allow tilt rotation in two directions, which is essential to the proper alignment of the microcantilever beams to the contact substrate. A Michelson interferometer is attached to the optical microscope (Leitz/Leica Camera AG) to generate alternating dark and light fringes, which are captured by a CCD camera (Panasonic GP-KR222). Since environmental humidity affects the contact and adhesion between the beam and substrate, the experimental setup is sealed in a chamber with humidity control and the entire apparatus is placed on a vibration isolation table.

Figure 4(c) shows the humidity control system. The  $\text{N}_2$  tank has three outlets, with one of them feeding dry  $\text{N}_2$  directly into the plastic mixing box. The other two dry  $\text{N}_2$  gas streams flow through the glass flask filled with water and thus pick up humidity. All three  $\text{N}_2$  gas streams are mixed in the mixing box and the temperature and humidity of the mixed  $\text{N}_2$  are monitored by a digital hydrothermometer. By adjusting the  $\text{N}_2$  flow rate for each stream using the flowmeters, the humidity of the mixed  $\text{N}_2$  that finally flows into the humidity chamber can be precisely controlled. The in-situ humidity and temperature in the chamber during the beam-peel-test are recorded by another digital hydrothermometer. For an intermediate humidity level, for example 70%, it takes up to one hour to reach a steady state in the humidity chamber.

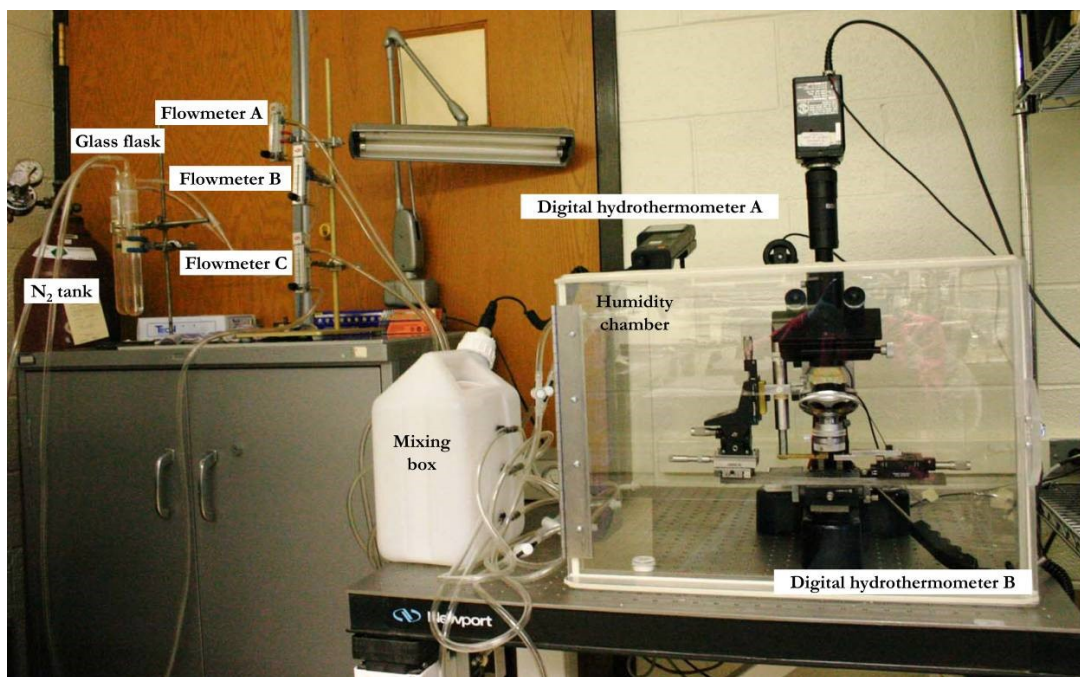
**Figure 4**



(a)



(b)



(c)

**Figure 4.** Experimental set-up. (a) Schematic, (b) close-up photograph, (c) photograph of humidity control system.

The proper alignment of the set-up is critical for the testing. As shown in Table 3, where the step-by-step experimental procedure is described, first the substrate is

positioned under the interferometer's objective. Then, the objective is adjusted to be parallel to the substrate until no fringes are observed on the substrate. Then, the substrate is moved away and the microcantilevers are brought into the field of view of the microscope. Goniometers are used to align the beam array parallel to the focal plane (no apparent fringes). At this point, the substrate, the beam array, and the objective focal plane should be parallel to each other. After alignment, the substrate is positioned about  $80\ \mu\text{m}$  below the beams using the linear Z stage. The piezoactuator is then used to lower the beam gradually by  $100\ \text{nm}$  decrements until the bottom surface of the beam is touching the substrate, which can be identified by the disappearance of the fringes on the microcantilevers, as shown in the actual interferometric image of Fig. 5(a) ( $h = 0\ \mu\text{m}$ ). The scale of the image is given by the two parallel diagonal mark lines ( $100\ \mu\text{m}$  marker).

**Table 3.** Experimental procedure for microcantilever peel experiments.

Step	Experimental Procedure
1	Align substrate parallel to objective
2	Align microcantilevers parallel to objective
3	Bring microcantilevers into contact with the substrate
4	Keep the constant humidity level for at least 12 hours to reach steady-state
5	Raise microcantilevers and measure the crack length when crack propagation occurs

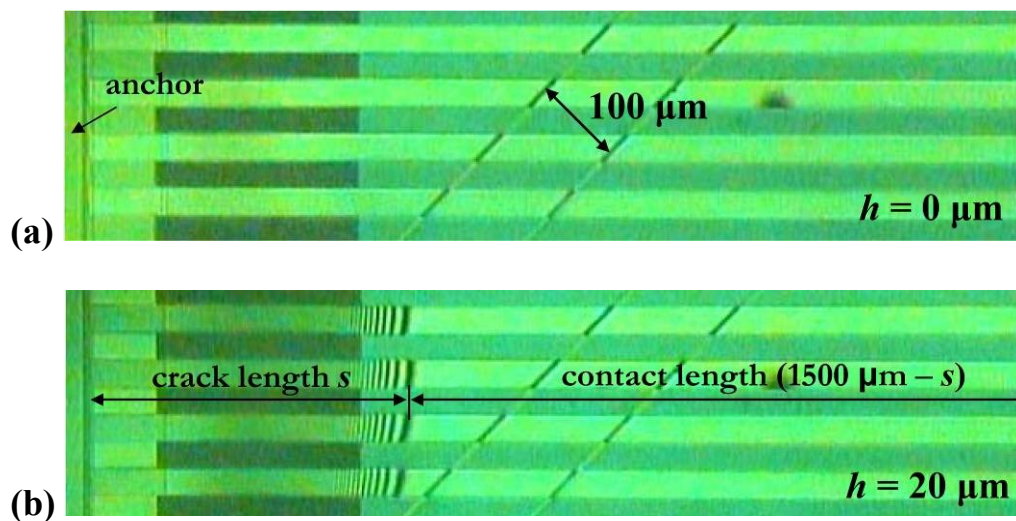


**Figure 5.** Interferometric images when (a) microcantilevers are contacting with the substrate,  $h = 0\ \mu\text{m}$ , (b) microcantilevers are  $20\ \mu\text{m}$  higher than the substrate,  $h = 20\ \mu\text{m}$  (the contact length is equal to the length of the microcantilever minus the crack length  $s$ ).

Typically, at a specified  $RH$  level, the beam array will take twelve or more hours of exposure in the chamber to reach equilibrium. Once the equilibrium is reached, the piezoactuator is used to raise the anchor of the beam in 100 nm increments. Due to the high compliance of the beam, the adhesion force between the bottom surface and the substrate will keep the free end of the beam into contact with the substrate over a considerable length, as shown in the schematic of Fig. 3(b). The Michelson interferometric attachment illuminates the samples with green (548 nm) light and provides alternating dark and light fringes that account for an out-of-plane deflection of 274 nm per fringe. A CCD camera is used to capture the interferometric images. The captured fringe density is directly related to the deflection profile of the microcantilever and the crack length can be readily determined from the images, as shown in Fig. 5(b). Equations (3) and (5) are then used to calculate the corresponding adhesion energy between the microcantilevers and the substrate. The microcantilevers are continuously raised until the beam breaks free from the substrate.

In the experimental set-up of this work, since the substrate and the microcantilever arrays are two separate parts, the microcantilevers and the substrate can be treated separately and different substrates can be tested and compared using the same microcantilevers at different humidity levels. Even though in this work the focus was on roughness effects, one could readily test substrates with coatings or other surface modifications.

### 2.3. Experimental results

Peel tests were performed on four different surface pairs at controlled humidity levels ranging from about 40% to 95%. Surface pair *a* is microcantilever *A* on silicon wafer substrate, pair *b* is microcantilever *B* on silicon wafer, pair *c* is microcantilever *A* on LPCVD deposited polysilicon substrate at 585 °C, and pair *d* is microcantilever *A* on polysilicon deposited at 590 °C. From geometrical considerations, the static contact between two rough surfaces can be modeled as the contact between an equivalent rough surface and a rigid flat surface [28]. The surface roughness parameters of the equivalent rough surface for each contact pair are listed in the bottom part of Table 2, and were extracted using the method described in [53]. It is seen that the surface roughness of the equivalent surfaces is dominated by the rougher surface of the contacting pair. For example, the roughness parameters of surface pair *b* are very close to those of microcantilever *B*.

Figure 6 depicts interferometric images taken for surface pair *a* (microcantilever *A* on silicon wafer substrate) at humidity levels of 90%, 80%, 70% and 45% when the microcantilever was positioned 20  $\mu\text{m}$  above the substrate. It can be seen that as the humidity decreases, the adhesion energy decreases, which

results in the increase of the measured crack length. For example, when the humidity is 90%, the crack length is only 366  $\mu\text{m}$ , which corresponds to an adhesion energy of 99.32  $\text{mJ}/\text{m}^2$ . When the humidity decreases to 45%, the crack length increases to 732  $\mu\text{m}$  and the corresponding adhesion energy is only 6.21  $\text{mJ}/\text{m}^2$ .

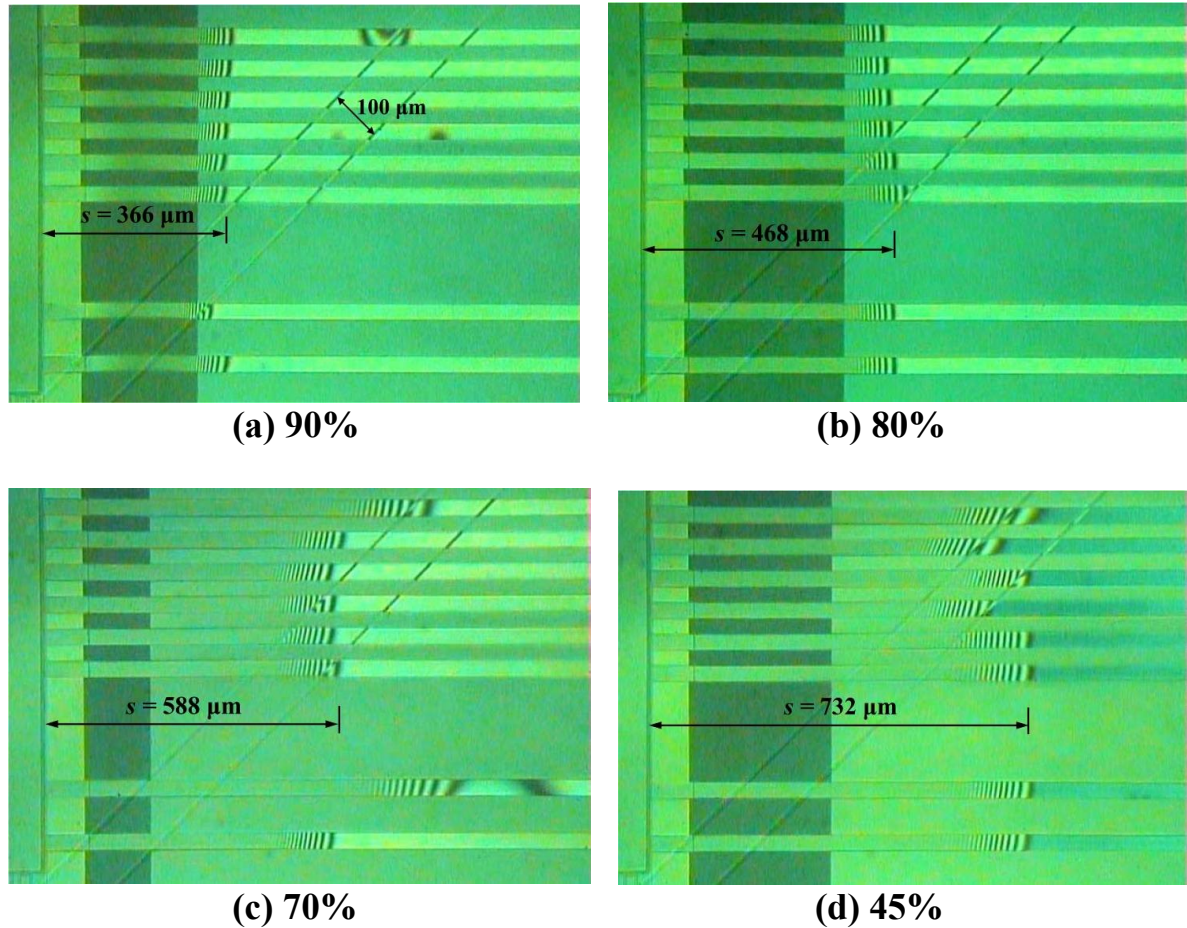


**Figure 6.** Interferometric images when microcantilevers are 20  $\mu\text{m}$  higher than the substrate for surface pair *a* at humidity levels of (a) 90%, (b) 80%, (c) 70%, and (d) 45% (*s* is the crack length).

Figure 7 depicts the average adhesion energy values measured on surface pairs *a*, *b*, and *c* for *RH* levels ranging from 44% to 92%. The error bars represent plus and minus one standard deviation of the measured adhesion energies when the beams were at different heights above the substrate. It is seen that for all surface roughness pairs, the adhesion energy between the bottom microcantilever surface and the substrate increases with increasing *RH* value. The smoother the surfaces are (pairs *a* and *b*), the higher the measured adhesion energy and also the lower the

dependence on  $RH$ . For example, when  $RH = 80\%$ , the adhesion energy for surface pair  $c$  ( $\sigma_{ab} = 5.7$  nm) is only  $0.47 \pm 0.09$  mJ/m<sup>2</sup>, while the adhesion energy of surface pair  $a$  ( $\sigma_{ab} = 1.7$  nm) is much higher at  $37.36 \pm 5.59$  mJ/m<sup>2</sup>. For surface pair  $d$ , due to its relatively high roughness, it was difficult to get s-shaped beams (i.e. pair  $d$  exhibited very low adhesion energy values), and no data is shown in this work.

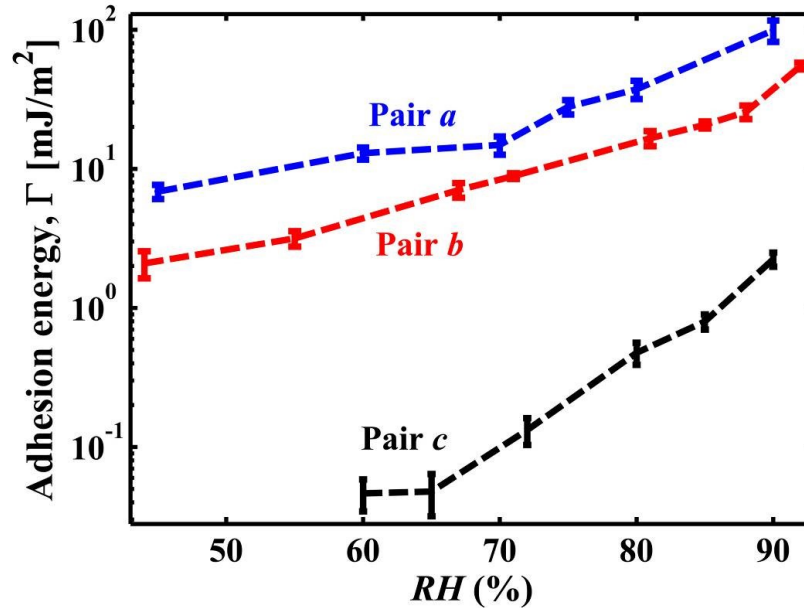


**Figure 7.** Average adhesion energy measured on surface pairs  $a$  ( $\sigma_{ab} = 1.5$  nm),  $b$  ( $\sigma_{ab} = 3.2$  nm), and  $c$  ( $\sigma_{ab} = 4.5$  nm) for  $RH$  ranging from 44% to 92% (parameters shown in Table 2,  $\sigma_{ab}$  = standard deviation of asperity heights of the equivalent rough surface).

### 3. Modeling

The static contact between two rough surfaces can be modeled as the contact between an equivalent rough surface and a flat rigid surface. In the presence of capillary condensation, menisci form around the asperities due to surface tension effects, as shown schematically in Fig. 8. By integrating the contribution of each asperity, the adhesion force and the contact load between the two rough surfaces can be determined. To calculate the single-asperity capillary force, the surface asperities can be treated as a deformable sphere of radius  $R$  contacting with a flat surface [28].

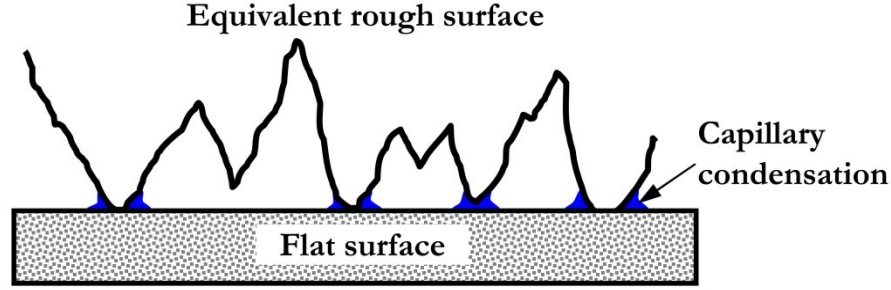


**Figure 8.** Schematic of a rough surface in contact with a rigid flat surface in the presence of capillary condensation.

### 3.1. Simplified single-asperity meniscus model

In most surface meniscus models that appear in the literature, the classical single-asperity equations presented by Israelachvili [36] are widely used, which do not take into account the spherical deformation caused by the adhesive force and repulsive contact force, i.e.

$$f_{m\_simplified} = \begin{cases} 4\pi R\gamma_{lv} \cos\theta \left(1 + \frac{\omega}{h_{lk}}\right) & \omega < 0 \\ 4\pi R\gamma_{lv} \cos\theta & \omega \geq 0 \end{cases}, \quad (6)$$

where  $\gamma_{lv}$  is the surface tension of the liquid-air interface,  $\theta$  is the contact angle,  $\omega$  is the interference,  $h_{lk}$  is the liquid film thickness estimated by the Laplace-Kelvin equation,

$$h_{lk} = \frac{2\gamma_{lv}V \cos\theta}{R_g T \ln(RH)}. \quad (7)$$

$V$  is the liquid molar volume,  $R_g$  is the gas constant, and  $T$  is the absolute temperature. For water at room temperature,  $\gamma_{lv}V/(R_g T) = 0.54$  nm.

### 3.2. Improved EMD-based single-asperity meniscus model

Maugis [60] and Johnson [61] pointed out that the Laplace pressure acting in a meniscus area is a “perfect” example of the Dugdale model. Xue and Polycarpou [44] developed an improved EMD-based single-asperity meniscus model, in which

the EMD theory is adopted to analyze the single-asperity adhesion behavior in the presence of capillary condensation. Instead of the approximation to the Lennard-Jones potential, the Dugdale stress is taken as the Laplace pressure acting on the wetted area. This improved EMD-based, single-asperity meniscus model considering both asperity deformation and solid surface interaction is coupled with the Pearson system of frequency curves to predict the contact and adhesion between two rough surfaces at different relative humidity levels.

### 3.2.1. Non-contacting asperity ( $\omega < 0$ )

For a non-contacting sphere ( $\omega < 0$ ) as shown in Fig. 9(a), the pressure inside the liquid is lower than that outside the liquid and the pressure difference  $\Delta p$  acting on the circular wetted area of radius  $c$  is given by the Laplace equation

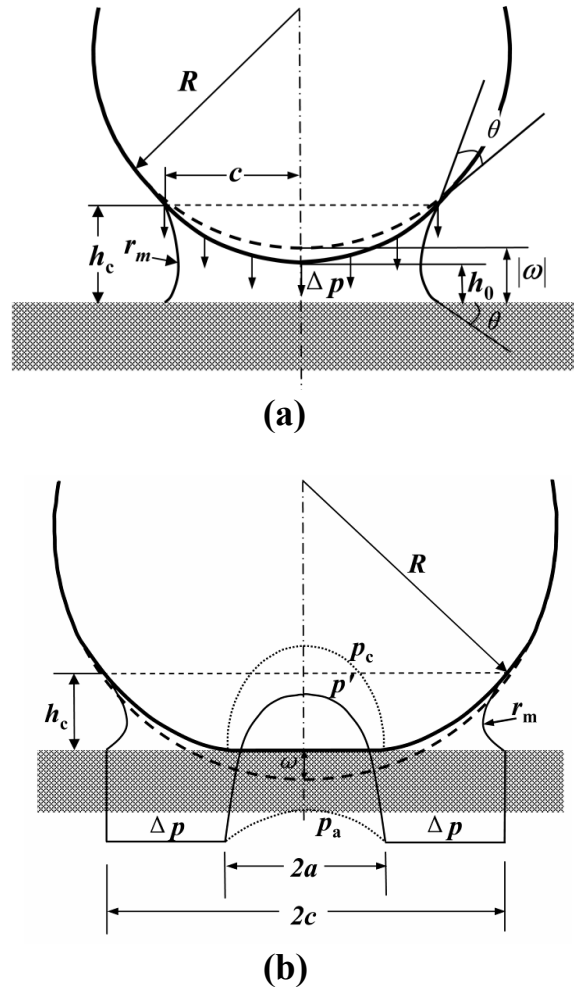


**Figure 9.** Schematic of a deformable elastic sphere and a rigid flat surface. (a) non-contacting  $\omega < 0$ , (b) contacting  $\omega > 0$ .

$$\Delta p = \frac{\gamma_{lv}}{r_m} = \frac{2\gamma_{lv} \cos \theta}{h_{lk}}, \quad (8)$$

where  $r_m$  is the meniscus radius. Assuming the displacement is negative in the departing direction, the radius of the projected meniscus area,  $c$ , can be obtained by solving the equation below:

$$\frac{c^2}{2R} + \frac{2\Delta p c (\pi - 2)}{\pi E_r} + h_0 - h_{lk} = 0, \quad (9)$$

where  $h_0$  is the normal separation at the center.  $E_r$  is the reduced elastic modulus defined by  $1/E_r = (1 - \nu_1^2)/E_1 + (1 - \nu_2^2)/E_2$ , where  $E_1$ ,  $E_2$ ,  $\nu_1$ , and  $\nu_2$  are Young's moduli and Poisson's ratios of the sphere and the flat surface, respectively. The Laplace pressure acts on the wetted area  $\pi c^2$ , pulling the sphere towards the substrate with an attractive force

$$f_m = \pi \Delta p c^2. \quad (10)$$

The thick dashed line in Fig. 9(a) shows the original spherical profile and the solid line represents the actual deformed shape. It can be seen that the sphere deforms towards the surface due to the attractive capillary force. The approach of the sphere is given by

$$\omega = h_0 + \frac{2c\Delta p}{E_r}. \quad (11)$$

### 3.2.2. Contacting asperity ( $\omega > 0$ )

Figure 9(b) shows a sphere contacting with a rigid surface ( $\omega > 0$ ), assuming the liquid is expelled from the contact region, allowing solid-to-solid contact. The constant Dugdale stress  $\Delta p$  (which is taken as the Laplace pressure) acts on the wetted area  $a < r < c$  up to a maximum separation  $h_{lk}$  beyond which it falls to zero. The induced Hertzian compressive pressure  $p_c(r)$  and the tensile adhesion pressure  $p_a(r)$  act inside the contact zone [60] and are given by:

$$\text{for } r < a, \begin{cases} p_c(r) = \frac{2E_r \sqrt{a^2 - r^2}}{\pi R} \\ p_a(r) = \frac{2}{\pi} \Delta p \tan^{-1} \left( \frac{c^2 - a^2}{a^2 - r^2} \right)^{1/2}. \end{cases} \quad (12)$$

When  $r = a$ , the stress is equal to  $\Delta p$ , which ensures stress continuity at the crack tip.

In the MD model [60], the “work of adhesion”  $w$ , defined as the external work done to separate a unit area of the adhering surfaces, is determined by the Lennard-Jones surface potential; whereas, in the current model, the effective work of adhesion is given by the value of the meniscus adhesion assuming no solid-solid interaction across the liquid (outside the contact region),

$$w = h_c \Delta p = 2r_m \cos \theta \frac{\gamma_{lv}}{r_m} = 2\gamma_{lv} \cos \theta. \quad (13)$$

The adhesion parameter,  $\lambda$ , can then be expressed as:

$$\lambda = \Delta p \left( \frac{9R}{2\pi w E_r^2} \right)^{1/3} = \frac{1}{r_m} \left( \frac{9R \gamma_{lv}^2}{4\pi \cos \theta E_r^2} \right)^{1/3}. \quad (14)$$

Letting  $m = c/a$ , the MD theory gives [60]

$$\frac{\lambda a^{*2}}{2} \left[ \sqrt{m^2 - 1} + (m^2 - 2) \tan^{-1} \sqrt{m^2 - 1} \right] + \frac{4\lambda^2 a^*}{3} \left[ \sqrt{m^2 - 1} \tan^{-1} \sqrt{m^2 - 1} - m + 1 \right] = 1, \quad (15)$$

where  $a^*$  is the normalized contact radius

$$a^* = a \left( \frac{4E_r}{3\pi w R^2} \right)^{1/3}. \quad (16)$$

One could also define a normalized asperity approach as:

$$\omega^* = \omega \left( \frac{16E_r^2}{9\pi^2 w^2 R} \right)^{1/3} = a^{*2} - \frac{4}{3} a^* \lambda \sqrt{m^2 - 1}. \quad (17)$$

The adhesion force due to the Laplace pressure outside the area of contact is obtained as

$$f_m = \Delta p \pi (c^2 - a^2) \text{ or } \frac{f_m}{\pi w R} = \frac{\pi}{2} \lambda a^{*2} (m^2 - 1). \quad (18)$$

For small  $\lambda$  values (as for example for the case of high humidity levels and small stiff spheres) the MD model becomes a “DMT-like” contact [62] where capillary condensation dominates the adhesion force. At low humidity levels and large compliant spheres,  $\lambda$  is large and the model predicts a “JKR-type” contact [63]. Note that Fogden and White [41] defined the transition from JKR-type to DMT-type contact using a similar adhesion parameter, which is related to the inverse of the parameter  $\lambda$ .

In the case of large  $\lambda$  values, the contribution of the adhesion force inside the contact region ( $r < a$ ) is also important and needs to be considered. Integrating the adhesion stress gives the adhesion force inside the contact region:

$$f_{s-s} = \int_0^a 2\pi r p_a(r) dr = 4\Delta p \int_0^a r \tan^{-1} \sqrt{\frac{c^2 - a^2}{a^2 - r^2}} dr. \quad (19)$$

The total adhesion force is obtained as

$$f_a = f_m + f_{s-s} = 2\Delta p a^2 \left( m^2 \tan^{-1} \sqrt{m^2 - 1} + \sqrt{m^2 - 1} \right). \quad (20)$$

Integrating the compressive stress gives the contact force:

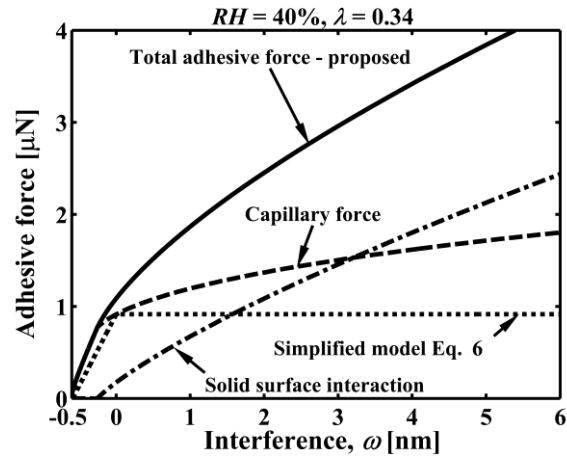
$$p = \int_0^a 2\pi r p_c(r) dr = \frac{4E_r a^3}{3R}. \quad (21)$$

Note that in this study, the effect of solid surface energy on the adhesion force is ignored and a constant  $\gamma_{lv}$  due to water is assumed.

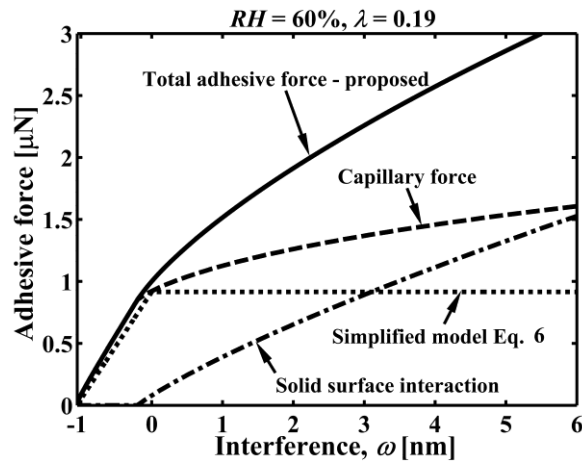
### 3.2.3. Effect of adhesion parameter $\lambda$

Figure 10 depicts adhesive forces as a function of interference at varying humidity levels of 40%, 60%, and 85% for a 2  $\mu\text{m}$  sphere radius on a rigid flat (the reduced modulus is 43 GPa and the contact angle is  $60^\circ$ ). Note that in this case the liquid thickness is estimated by Eq. (7). The simplified model predicts a constant adhesive force for contacting spheres ( $\omega > 0$ ) independent of the relative humidity and sphere interference as it ignores the spherical deformation and the contribution from inside the contact zone, while the EMD-based meniscus model shows an increase of the adhesive force with the spherical interference. At low humidity levels,  $\lambda$  is larger and the EMD-based model shows a JKR-like contact. As shown in Fig. 10(a), for non-contacting conditions ( $\omega < 0$ ), due to the spherical deformation, the induced capillary force is higher than that predicted by Eq. (6) and the sphere will touch the solid surface when they are brought into close proximity. When the sphere makes contact with the substrate ( $\omega > 0$ ), the adhesive force due to solid surface interaction inside the contact region arises and increases with increasing interference (contact area). Meanwhile, the capillary force increases with interference due to the spherical deformation. Thus, the total adhesive force (capillary force plus solid surface force) is higher than that predicted by the simplified model (Eq. (6)) in which case the maximum force is reached at the onset of contact ( $\omega = 0$ ) and a constant value is assumed thereafter (for the contacting asperities ( $\omega > 0$ )).

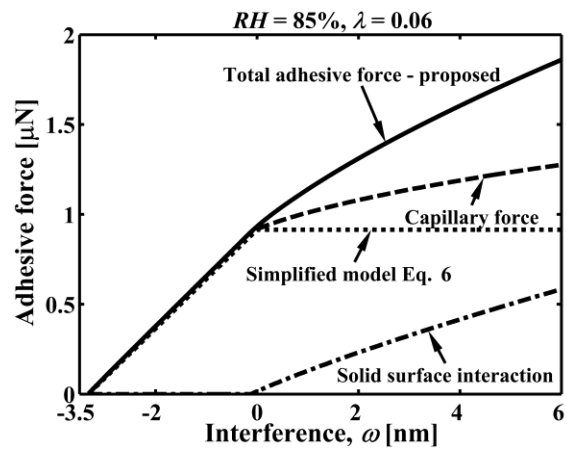
As humidity increases, the  $\lambda$  value becomes smaller and the EMD-based model shows more of a DMT-like contact behavior. As shown in Fig. 10(c), for the non-contacting sphere ( $\omega < 0$ ) the adhesion force difference caused by the spherical deformation is very minor, and for the contacting case, the contribution of the adhesion force from inside the contact zone is much smaller than that at the low humidity level. It is also seen in Fig. 10, that for contacting asperities ( $\omega > 0$ ), lower relative humidity results in higher meniscus forces at the same interference. This is because the Laplace pressure acting on the sphere surface by the condensed liquid is lower at the higher humidity, and the increase of the wetted area is not as fast as that at the lower humidity.



(a)



(b)



(c)

**Figure 10.** Adhesive forces versus interference for a sphere on a rigid flat surface ( $R = 2 \mu\text{m}$ ,  $\theta = 60^\circ$ ) at varying relative water vapor pressures of: (a) 0.4, (b) 0.6, and (c) 0.85.

### 3.3. EMD-Pearson meniscus surface model

By incorporating the single-asperity meniscus model in the GW statistical model [28] the adhesion force and adhesion energy between two rough surfaces can be obtained. Note that in this work we use a statistical surface model, which is justified based on the roughness measurements presented above. The basic single-asperity meniscus model presented above is generally applicable and could also be used with other surface roughness models, such as the fractal model [64]. For a rough surface with multi-asperity contact interface, the net adhesion force arises from the individual asperity contributions. According to the GW model, the surface topography of the equivalent rough surface can be characterized by three parameters, namely  $\sigma$ ,  $\eta$ ,  $R$ , and that the asperity heights  $z$  follow a probability density function. In most meniscus surface models, a Gaussian (symmetric) distribution is usually assumed, given by

$$\phi(z) = \frac{1}{\sigma_{ab} \sqrt{2\pi}} e^{-0.5(z/\sigma)^2}. \quad (22)$$

However, as clearly seen in Table 2, MEMS surfaces do not typically exhibit a Gaussian distribution. To describe an asymmetric non-Gaussian surface, two statistical parameters, the skewness and kurtosis, representing the asymmetry and flatness of the asperity height distribution are used. Several different types of non-Gaussian height distributions have been proposed including the Weibull distribution [57] and the Pearson system of frequency curves [65]. Although the Weibull distribution is mathematically attractive and can represent asymmetric distributions, the effects of kurtosis and skewness are coupled and cannot be studied independently. By generating the exact probability density function of the asperity heights using the measured four moments, i.e., mean, standard deviation, skewness, and kurtosis, the Pearson system of frequency curves [65] can be used to study the effect of skewness and kurtosis independently.

Table 4 lists the probability density functions of different types of Pearson surfaces [65]. The Pearson parameter,  $\kappa$ , is used to determine the type of the surface distribution:

$$\kappa = \frac{S_{sk}^2 (S_{ku} + 3)^2}{4(2S_{ku} - 3S_{sk}^2 - 6)(4S_{ku} - 3S_{sk}^2)}. \quad (23)$$

**Table 4.** Probability density functions using the Pearson system of frequency curves.

Type		Criterion	Equations with origin at the mean
Main types	I	$-\infty < \kappa < 0$	$\phi(z) = y_0 \left(1 + \frac{z}{A_1}\right)^{m_1} \left(1 - \frac{z}{A_2}\right)^{m_2} \quad (-A_1 < z < A_2)$
	IV	$0 < \kappa < 1$	$\phi(z) = y_0 \left(1 + \left(\frac{z-v}{a} - \frac{v}{r}\right)^2\right)^{-m} \exp\left(-v \tan^{-1}\left(\frac{z-v}{a} - \frac{v}{r}\right)\right)$
	VI	$1 < \kappa < \infty$	$\phi(z) = y_0 \left(1 + \frac{z}{A_1}\right)^{-q_1} \left(1 + \frac{z}{A_2}\right)^{q_2}$
Transition types	Normal	$\kappa = 0, S = 0, K = 3$	$\phi(z) = y_0 \exp\left(-\frac{z^2}{2\sigma^2}\right)$
	II	$\kappa = 0, S = 0, K < 3$	$\phi(z) = y_0 \left(1 - \frac{z^2}{a^2}\right)^m \quad (-a < z < a)$
	VII	$\kappa = 0, S = 0, K > 3$	$\phi(z) = y_0 \left(1 + \frac{z^2}{a^2}\right)^{-m}$

Equations for curve fitting parameters ( $y_0, A, A_1, A_2, m, m_1, m_2, a, v, r, q_1, q_2$ ) can be found in [65].

Integrating the capillary force at each surface asperity, the meniscus force between two rough surfaces can be obtained as

$$F_m = A_n \eta \int_{d-h_k}^{\infty} f_m \phi(z) dz, \tag{24}$$

where  $A_n$  is the nominal area of contact at a rough interface and  $\phi(z)$  is the Pearson distribution given in Table 4.

To calculate the total adhesion force at low and intermediate  $RH$  levels, in addition to the contribution of capillary condensation, the solid surface interaction inside the contact zone is also included as follows

$$F_{s-s} = A_n \eta \int_{d-h_k}^{\infty} f_{s-s} \phi(z) dz, \tag{25}$$

and the total adhesion force between two contacting rough surfaces is obtained by

$$F_a = F_m + F_{s-s}. \quad (26)$$

At equilibrium, an external force  $F$  separating the surfaces must be applied

$$F = P - F_a, \quad (27)$$

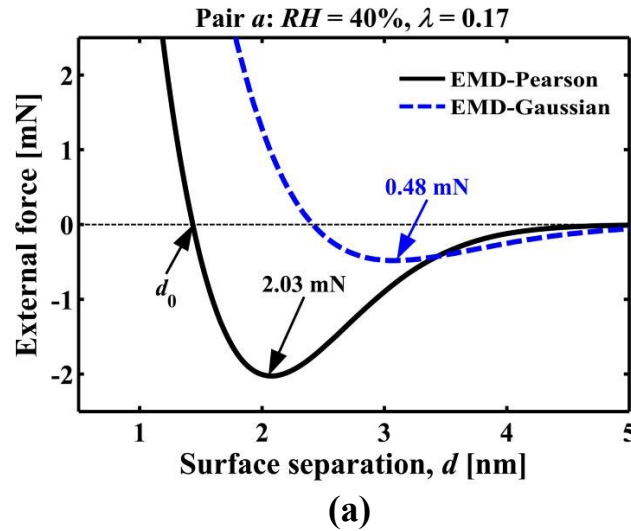
where  $P$  is the asperity contact deformation force calculated by

$$P = A_n \eta \int_{d-h_k}^{\infty} p\phi(z) dz, \quad (28)$$

and the pull-off force is defined as the minimum value of the external force.

Figure 11 depicts the external force as a function of surface separation for surface pair  $a$  at  $RH$  of 40%, 70%, and 85%. It is seen that when the humidity increases from 40% to 85%, the corresponding pull-off force also increases. In addition, at the high humidity level, the force estimated using a Gaussian distribution (13.2 mN) is close to that predicted by the Pearson distribution (15.45 mN). As the humidity decreases, the Gaussian distribution greatly underestimates the pull-off force. For example, at  $RH = 40\%$ , the Gaussian distribution predicts 0.48 mN at  $d = 3.1$  nm, while the Pearson distribution predicts 2.03 mN at  $d = 2.05$  nm.

**Figure 11**



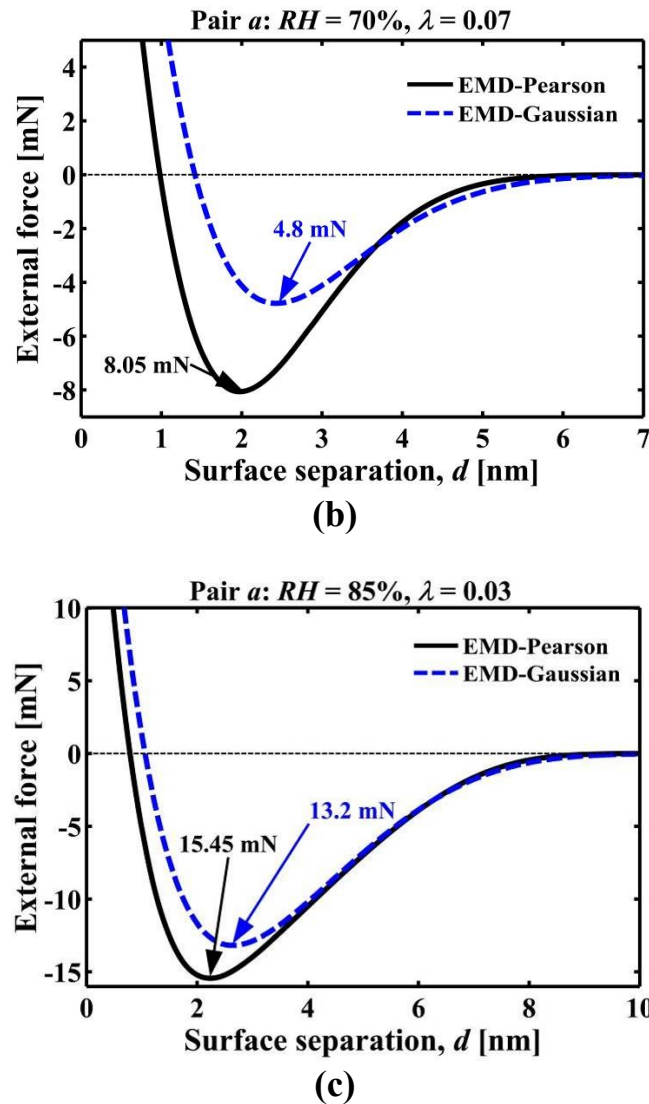


**Figure 11.** External force versus surface separation for surface pair *a* at humidity levels of (a) 40%, (b) 70%, and (c) 85%.  $d_0$  is the equilibrium point at zero applied load,  $\lambda$  is the adhesion parameter given by Eq. (14).

To examine the effects of using an inaccurate asperity distribution, the histogram of the surface heights for the bottom surface of microcantilever *A* was extracted using the measured AFM data as shown in Fig. 12. Note that in surface pair *a*, since the microcantilevers are much rougher than the silicon substrate, the adhesion force is primarily determined by the bottom surface of the microcantilevers. The fitted Pearson and Gaussian distributions are also shown in the figure. It is seen that the distribution generated using the Pearson system matches the actual surface better than the Gaussian distribution. This is because the Pearson system uses more fitting parameters which capture both the asymmetry

and flatness of the surface heights, while the symmetric Gaussian distribution simply fits the data with  $S_{sk} = 0$  and  $S_{ku} = 3$ .

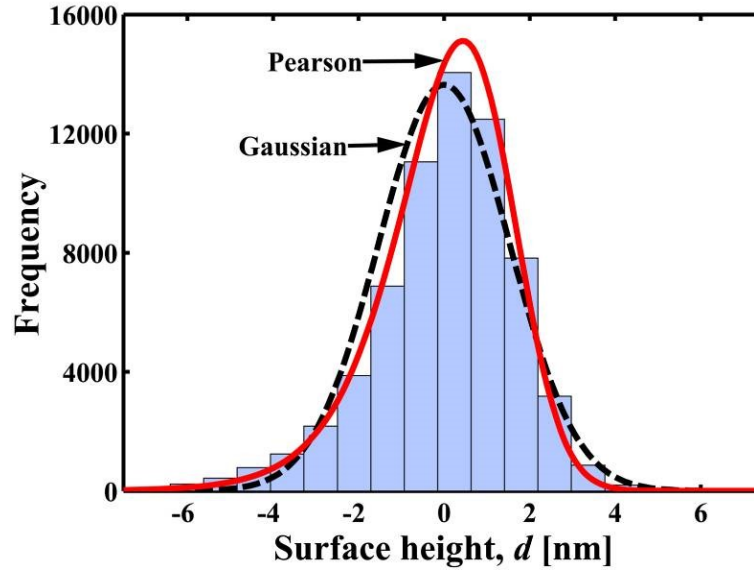


**Figure 12.** Histograms with Gaussian and Pearson distribution fits of the surface roughness of bottom surface of microcantilever *A*.

At low humidity levels, the thickness of the condensed liquid is small and only the highest asperities on the surface affect the adhesion behavior. The Gaussian distribution predicts more asperities contact with the substrate (compared to the actual surface) and thus overestimates the surface separation at contact and underestimates the pull-off force. At high *RH*, the condensed liquid is thicker and the contact and adhesion behavior of the surface is determined by the majority of asperities, thus the difference caused by the distribution is not as significant as at the low humidity, as shown in Fig. 11.

### 3.4. Comparison between model and experiments

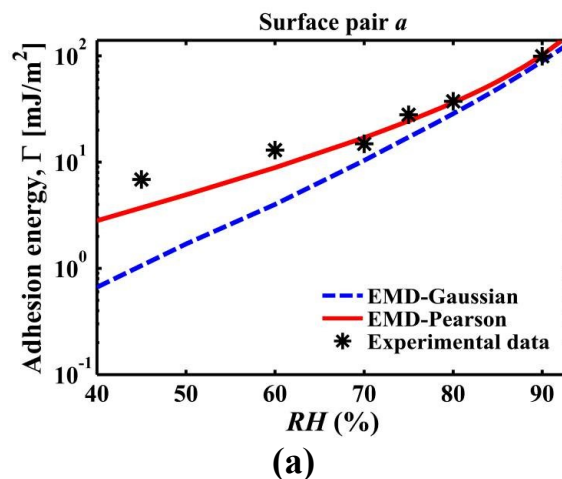
To calculate the adhesion energy per unit area ( $\text{mJ/m}^2$ )  $\Gamma$  from the modeled predictions, the force-displacement curves shown in Fig. 11 were integrated from the equilibrium point  $d_0$  (at zero applied load) to infinity,

$$\Gamma = \frac{1}{A_n} \int_{d_0}^{\infty} F(d) dd, \quad (29)$$

where  $F$  is the total external force given by Eq. (27).

Figure 13 shows measured and modeled adhesion energy  $\Gamma$  as a function of  $RH$  for three of the surface pairs. The solid line represents the EMD-based Pearson meniscus model and the dashed line is the EMD-based-Gaussian meniscus model. It is seen that by generating the exact asymmetric surface topography, the Pearson-based model matches the experimental data very well from low humidity to high humidity for surface pairs  $a$  and  $b$ , while the Gaussian-based model greatly underestimates the adhesion energy at low  $RH$ . For example, for surface pair  $b$  (shown in Fig. 13(b)), when  $RH = 44\%$ , the measured energy is  $2.09 \text{ mJ/m}^2$  and the predicted energy using the correct Pearson model is  $0.93 \text{ mJ/m}^2$  while the Gaussian-based model gives an unrealistic low value of  $0.0015 \text{ mJ/m}^2$ . Also, it is seen that both models work better for smoother surfaces and higher humidity levels. As the surface roughness increases, the difference between model and experimental results increases. This is possibly because in the improved EMD single-asperity meniscus model, the solid surface interaction within the contact zone was calculated by integrating the induced adhesion stress within the contact region due to the Laplace pressure instead of the surface energy of the solid surface [44]. Also note that in this study, we assume a constant  $\gamma_{lv}$  due to water. In fact, at very low humidity levels, the surface tension of the liquid could be altered by the solid surface, as shown for example in the case of molecularly thin perfluoropolyether lubricants in magnetic storage [66]. However, no similar analysis exists for water vapor.

**Figure 13**



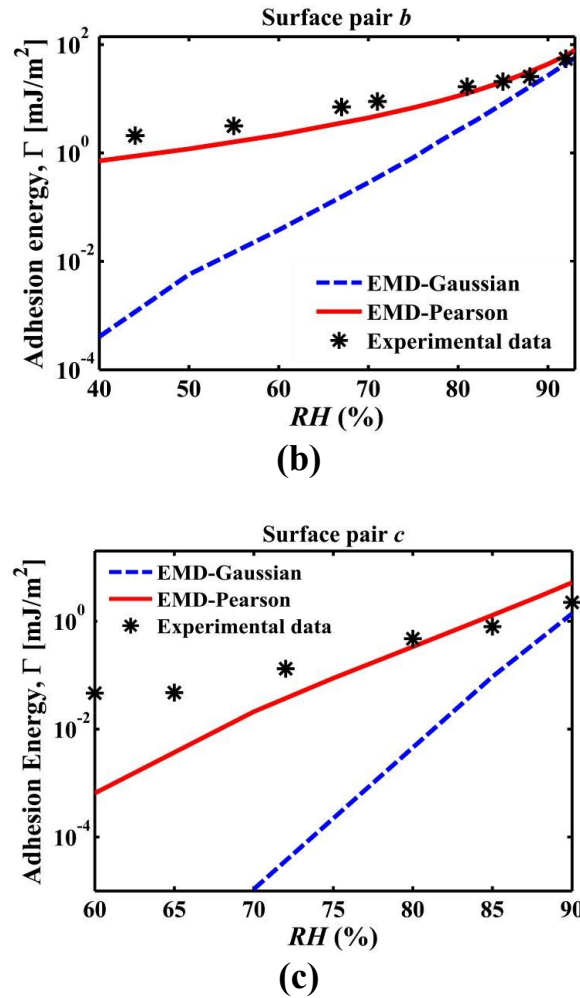


**Figure 13.** Comparison between measured and modeled adhesion energies  $\Gamma$  versus  $RH$  for (a) surface pair  $a$ , (b) surface pair  $b$ , (c) surface pair  $c$ .

The good agreement between the experimental and model results for low roughness and high humidity conditions demonstrates that statistical representation of the surfaces enables accurate predictions of adhesion energy for these conditions. Since the proposed model is based on the generalized EMD model, which is valid for a wide range of adhesion parameter values, it is applicable to other material systems, including soft materials (large adhesion parameter values). Through incorporating the effect of solid surface energy and also considering the plastic asperity deformation, the applicability of the model would likely be extended to higher surface roughness at lower humidity.

## 4. Summary

MEMS design and fabrication have significantly improved, yet adhesion and contact are major reliability concerns and thus an obstacle to widespread use of such miniature devices. In this chapter, MEMS-scale beam-peel-test experimental set-up was developed and microcantilever beam arrays fabricated by different runs were used to measure the adhesion energy of substrates with different roughness values at controlled humidity levels from 40% to 92%. It was found that the adhesion energy and pull-off force increased with increasing  $RH$  and decreasing surface roughness. The adhesion behavior was determined by the rougher surface of the contact pair. A EMD-based meniscus single-asperity adhesive model was coupled with the Pearson system of frequency curves to develop an improved asymmetrical surface meniscus model, which considers the asperity deformation and the adhesion contribution of surface interaction. The model works well from low humidity to high humidity range. Both the beam bottom surface and the substrates were scanned using AFM before the experiments and the extracted surface roughness parameters were used to generate the exact surface topography and input into the model for simulation. The model and the experimental data were favorably compared. The Pearson-based meniscus surface model matches with the experimental data very well from low  $RH$  to high  $RH$  for both surface pairs  $a$  and  $b$ , while the Gaussian-based model greatly underestimates the adhesion energy at the low  $RH$ . The proposed and validated continuum-based adhesive contact model is only a function of the surface roughness and material properties of the interacting surfaces, and does not include empirical coefficients. Moreover, the model is valid for a wide range of adhesion parameter values, covering the practical range of application of MEMS and other miniature devices.

## Acknowledgements

This work was supported by the National Science Foundation under grant number CAREER CMS-0239232. The authors acknowledge Dr. Leslie M. Phinney, Sandia National Laboratories, for providing the MEMS samples and valuable discussions. The authors acknowledge Professor Thomas J. Mackin, California Polytechnic State University, for initial discussions in regards to the experimental set-up. AFM measurements were conducted in the Center for Microanalysis of Materials, University of Illinois, which is partially supported by the U.S. Department of Energy under grant DEFG02-91-ER45439.

## References

1. Bustillo, J.M., Howe, R.T., and Muller, R.S. 1998. *Proc. IEEE*, **86**, 1552.
2. Maboudian, R. 1998. *Surf. Sci. Rep.*, **30**, 207.
3. de Boer, M.P., Clews, P.J., Smith, B.K., and Michalske, T.A. 1998. *Mater. Res. Soc. Proc.*, **518**, 131.
4. Tanner, D.M., Miller, W.M., Eaton, W.P., Irwin, L.W., Peterson, K.A., Dugger, M.T., Senft, D.C., Smith, N.F., Tangyunyong, P., and Miller, S.L. 1998. *Proc. IEEE 36th Annu. Int. Reliability Physics Symp.*, p. 26.
5. van Kessel, P.F., Hornbeck, L.J., Meier, R.E., and Douglass, M.R. 1998. *Proc. IEEE*, **86**, 1687.
6. Hartzall, A. and Woodilla, D. 1999. *Proc. IEEE 37th Annu. Int. Reliability Physics Symp.*, pp. 202-205.
7. Majumder, S., Mcgruer, N.E., Adams, G.G., Zavracky, P.M., Morrison, R.H., and Krim, J. 2001. *Sensor Actuat. A*, **93**, 19.
8. Kaajakari, V., Kan, S.H., Lin, L., Lal, A., and Rodgers, M. 2000. *Proc. SPIE*, 4180, 60.
9. Komvopoulos, K. 1996. *Wear*, **200**, 305.
10. Maboudian, R., and Carraro, C. 2004. *Annu. Rev. Phys. Chem.*, **55**, 35.
11. Xue, X., Polycarpou, A.A., and Phinney, L.M. 2008. *J Adhes. Sci. Technol.*, **22**, 429.
12. Alley, R.L., Mai, P., Komvopolous, K., and Howe, R.T. 1993. *Proc. 7th Int. Conf. Solid-State Sens. Actuators, Transducers '93, Japan*, p. 288.
13. Abe, T., Messner, W.C., and Reed, M.L. 1995. *Proc. IEEE Micro Electro Mechanical Systems Conf., Amsterdam, The Netherlands*, p. 94.
14. Dugger, M.T. 2005, *Proc. World Tribology Congress III, Washington D.C.*, p. 711.
15. Gao, D., Carraro, C., Howe, R.T., and Maboudian, R. 2006. *Tribology Lett.*, **21**, 226.
16. Rogers, J.W. and Phinney, L.M. 2001. *J. Microelectromech. Syst.*, **10**, 280.
17. Gogoi, B.P., and Mastrangelo, C.H. 1995. *J. Microelectromech. Syst.*, **4**, 185.
18. Christenson, H.K. 1988. *J. Colloid Interface Sci.*, **121**, 170.
19. Mate, C.M., McClelland, G.M., Erlandsson, R., and Chiang, S. 1987. *Phys. Rev. Lett.*, **59**, 1942.
20. Mastrangelo, C.H., and Hsu, C.H. 1992. *Proc. IEEE Solid-State Sens. Actuator Workshop, Hilton Head*, p. 208.
21. de Boer, M.P., and Michalske, T. 1999. *J. Appl. Phys.*, **86**, 817.
22. DelRio, F.W., Dunn, M.L., Phinney, L.M., Bourdon, C.J., and de Boer, M.P. 2007. *Appl. Phys. Lett.*, **90**, 163104.
23. Jones, E.E., Begley M.R., and Murphy, K.D. 2003. *J. Mech. Phys. Solids*, **51**, 1601.
24. Leseman, Z.C., Carlson, S., Xue, X., and Mackin, T.J. 2006. *Proc. ASME Intl Mech. Eng. Congress and Expo.*, Paper No. IMECE2006-14498, Chicago, IL.
25. Legtenberg, R., Tilmans, A.C., Elders, J., and Elwenspoek, M. 1994. *Sensor Actuat. A*, **43**, 230.
26. Alley, R.L., Cuan, G.J., Howe, R.T., and Komvopoulos, K. 1992. *Proc. IEEE Solid-State Sens. Actuator Workshop, Hilton Head*, pp. 202-207.
27. Ashurst, W.R., de Boer, M.P., Carraro, C., and Maboudian, R. 2003. *Appl. Surf. Sci.*, **212-213**, 735.

28. Greenwood, J.A., and Williamson, J.B.P. 1966. *Proc. Roy. Soc. Lond. Ser. A*, **295**, 300.
29. Chang, W.R., Etsion, I., and Bogy, D.B., 1988. *J. Tribology*, **110**, 50.
30. Muller, V.M., Yushchenko, V.S., and Derjaguin, B.V. 1983. *J. Colloid Interface Sci.*, **92**, 92.
31. Kogut, L., and Etsion, I. 2004. *J. Tribology*, **126**, 34.
32. Kogut, L., and Etsion, I. 2003. *J. Colloid Interface Sci.*, **261**, 372.
33. Shi, X., and Polycarpou, A.A. 2005. *J. Colloid Interface Sci.*, **281**, 449.
34. Lee, S.C. 2004, *Microtribodynamics of Sub-Five Nanometers Flying Head-Disk Interfaces in Magnetic Storage*, Ph.D. Thesis, University of Illinois at Urbana-Champaign, Urbana, Illinois, USA.
35. Shi, X., and Polycarpou, A.A. 2005. *J. Colloid Interface Sci.*, **290**, 514.
36. Israelachvili, J. 1985, *Intermolecular and Surface Forces*, Academic Press, San Diego.
37. Li, Y., and Talke, F.E. 1990. *Tribology and Mechanics of Magnetic Storage Systems*, B. Bhushan (Ed.) (STLE, Park Ridge, IL) Vol. VII, *STLE Special Publications SP-29*, pp. 79-84.
38. Tian, H., and Matsudaira, T. 1993. *ASME J. Tribology*, **115**, 28.
39. Gao, C., Tian, X., and Bhushan, B. 1995. *Tribology Trans.*, **38**, 201.
40. Gui, J., and Marchon, B. 1995. *J. Appl. Phys.*, **78**, 4206.
41. Fogden, A., and White, L.R. 1990. *J. Colloid Interface Sci.*, **138**, 414.
42. Zhang, B., and Nakajima, A., 1999. *J. Colloid Interface Sci.*, **211**, 114.
43. Xue, X., and Polycarpou, A.A. 2008. *J. Appl. Phys.*, **103**, 023502.
44. Xue, X., and Polycarpou, A.A., 2007. *J. Colloid Interface Sci.*, **311**, 203.
45. Stanley, H.M., Etsion, I., and Bogy, D.B. 1990. *ASME J. Tribology*, **112**, 98.
46. Suh, A.Y., Lee, S.C., and Polycarpou, A.A. 2006. *ASME J. Tribology*, **128**, 801.
47. Hegde, R.I., Paulson, W.M., and Tobin, P.J. 1995. *J. Vac. Sci. Technol. B*, **13**, 1434.
48. Sundararajan, S., and Bhushan, B. 2001. *J. Vac. Sci. Technol. A*, **19**, 1777.
49. Xue, X., and Phinney, L.M. 2003. *Proc. SPIE*, 4980, 130.
50. Xue, X., Koppaka, S.B., Phinney, L.M., and Mackin, T.J. 2004, *SEM International Congress & Exposition on Experimental & Applied Mechanics*, Paper No. 305, pp. 1-7.
51. Sniegowski, J.J., and de Boer, M.P. 2000. *Annu. Rev. Mater. Sci.*, **30**, 299.
52. Voutsas, A.T., and Hatlis, M.K. 1992. *J. Electrochem. Soc.*, **139**, 2659.
53. Xue, X., Phinney, L.M., and Polycarpou, A.A. 2008. *Microsyst Technol.*, **14**, 17.
54. Suh, A.Y., and Polycarpou, A.A. 2006. *Wear*, **260**, 538.
55. Yu, N., and Polycarpou, A.A. 2004. *ASME J. Tribology*, **126**, 225.
56. McCool, J.I. 1987. *ASME J. Tribology*, **109**, 264.
57. Yu, N., and Polycarpou, A.A. 2002. *ASME J. Tribology*, **124**, 367.
58. Rogers, J.W., Mackin, T.J., and Phinney, L.M. 2002. *J. Microelectromech. Syst.*, **11**, 512.
59. Schennum, S. 1995, *An Experimental and Theoretical Investigation of Delamination Resistance in Glass Fiber Reinforced Polyestere Laminates*, M.S. Thesis, University of Illinois at Urbana-Champaign, Urbana, Illinois, USA.
60. Maugis, D. 1992. *J. Colloid Interface Sci.*, **150**, 243.
61. Johnson, K.L., 1998. *Tribology Int.*, **31**, 413.
62. Derjaguin, B.V., Muller, V.M., and Toporov, Yu.P. 1975. *J. Colloid Interface Sci.*, **53**, 314.

63. Johnson, K.L., Kendall, K., and Roberts, A.D. 1971. *Proc. R. Soc. London Ser. A*, **324**, 301.
64. Komvopoulos, K. 2003. *J. Adhesion Sci. Technol.*, **17**, 477.
65. Elderton, W.P., and Johnson, N.L. 1969. *System of Frequency Curves*, Cambridge University Press, Cambridge, UK.
66. Tyndall, G.W., Leezenberg, P.B., Waltman, R.J., and Castenada, J. 1998. *Tribology Letters*, **4**, 103.